

A generalized wall-pressure spectral model for non-equilibrium boundary layers

Saurabh Pargal^{1,2}, Junlin Yuan^{1†} and Stephane Moreau²

¹Michigan State University, Michigan, USA

²Université de Sherbrooke, Quebec, Canada

(Received xx; revised xx; accepted xx)

This study uses high-fidelity simulations (DNS or LES) and experimental datasets to analyse the effect of non-equilibrium streamwise mean pressure gradients (adverse or favourable), including attached and separated flows, on the statistics of boundary layer wall-pressure fluctuations. The datasets collected span a wide range of Reynolds numbers (Re_θ from 300 to 23,400) and pressure gradients (Clauser parameter from -0.5 to 200). The datasets are used to identify an optimal set of variables to scale the wall pressure spectrum: edge velocity, boundary layer thickness, and the peak magnitude of Reynolds shear stress. Using the present datasets, existing semi-empirical models of wall-pressure spectrum are shown unable to capture effects of strong, non-equilibrium adverse pressure gradients, due to inappropriate scaling of wall pressure using wall shear stress, calibration with limited types of flows, and dependency on model parameters based on friction velocity, which reduces to zero at the detachment point. To address these shortcomings, a generalized wall-pressure spectral model is developed with parameters that characterize the extent of the logarithmic layer and the strength of the wake. Derived from the local mean velocity profile, these two parameters inherently carry effect of the Reynolds number, as well as those of the non-equilibrium pressure gradient and its history. Comparison with existing models shows that the proposed model behaves well and is more accurate in strong-pressure-gradient flows and in separated-flow regions.

Key words:

† Email address for correspondence: junlin@msu.edu

1. Introduction

The fluctuation in time of the wall pressure beneath a turbulent boundary layer is one of the major sources of flow-induced noise and vibrations. Accurate modeling of the statistics of wall-pressure fluctuations is important for noise prediction in a wide range of applications such as wind turbines (Avalone *et al.* 2018; Deshmukh *et al.* 2019; Venkatraman *et al.* 2023), cooling fans (Sanjosé & Moreau 2018; Swanepoel *et al.* 2023; Luo *et al.* 2020), propellers (Lallier-Daniels *et al.* 2021; Casalino *et al.* 2021), unmanned/manned air vehicles or drones (Lauzon *et al.* 2023; Pargal *et al.* 2023; Celik *et al.* 2021), and cabin noise (Samarasinghe *et al.* 2016; Borelli *et al.* 2021), etc., as well as for prediction of flow-induced structure fatigue (Franco *et al.* 2020). In these applications, the boundary layer flows are often turbulent and non-equilibrium, due to surface curvature and significant pressure gradients that vary in the streamwise direction, which may induce boundary layer separation and can be found in a large range of Reynolds number. Therefore, the generation of noise in non-equilibrium turbulent boundary layers is physically complex and challenging to model.

The modeling of wall-pressure loading as a noise source predominantly depends on the power spectral density (PSD) of wall-pressure fluctuations, as well as its spanwise correlation length and the convection velocity of turbulent structures (Amiet 1976; Roger & Moreau 2005; Moreau & Roger 2009; Lee *et al.* 2021). The focus here is on modeling wall-pressure spectrum (WPS). It is established that the WPS of a boundary layer with zero or minimal pressure gradient consists of three ranges (Goody 2004; Farabee & Casarella 1991; Chang III *et al.* 1999): (i) a range with ω^2 variation at low frequencies (where ω is the frequency), (ii) a range with ω^{-5} behavior at high frequencies, and (iii) an overlap range with a ω^{-1} decay rate between the above two ranges. Based on data primarily in equilibrium flows, the width of the overlap range was found to increase with Reynolds number (Farabee & Casarella 1991; Goody 2004).

Contributions from different layers of wall turbulence to the WPS has been studied

and are summarized below. The experimental studies of Farabee & Casarella (1991) suggested different dominant sources for different wavenumber ranges of the WPS: the high-wavenumber range is mainly attributed to turbulent activities in the logarithmic region, while the low-wavenumber range is attributed to large-scale turbulent motions in the outer layer. Van Blitterswyk & Rocha (2017) quantified the correlations between the fluctuations of wall pressure and those of velocity in different layers of boundary layer and observed that high-frequency and overlap ranges of the WPS are associated with flows in the buffer and logarithmic regions, respectively. As opposed to earlier studies performed on channel flow or canonical flat-plate boundary layer data, Jaiswal *et al.* (2020) analyzed data collected near the trailing edge of a cambered airfoil with a strong mean adverse pressure gradient (APG) in a highly non-equilibrium turbulent boundary layer, to compare contributions from various velocity sources at different wall-normal locations to the wall-pressure fluctuations based on the pressure Poisson's equation. They found that the mean shear (MS) term in the inner and logarithmic regions is the dominant contributor, especially in the mid-to-high frequency range.

Past studies were mostly on zero-pressure-gradient (ZPG) turbulent boundary layers. They showed that the wall-pressure fluctuations are intensified under a higher Reynolds number, mainly due to the increase in overlap-range spectral contribution. For a ZPG flat-plate boundary layer, Farabee & Casarella (1991) integrated the pressure spectrum over various frequency ranges and showed that the low-to-mid frequency range and the high-frequency range were not sensitive to a change in Reynolds number, whereas the significance of the overlap range increases with Reynolds number, leading to an augmentation of p_{rms} . They proposed that $p_{rms}^2/\tau_w^2 = 6.5 + 1.86 \ln(Re_\tau/333)$, which was tested with ZPG boundary layer and channel flow data. Panton & Linebarger (1974) also demonstrated that the overlap range is correlated with the Reynolds number.

The current understanding of the WPS in non-zero pressure gradient flows is summarized as follows. Review of the earlier work before the mid 1990s are provided by Willmarth (1975) and Bull (1996). Schloemer (1967) showed that under an APG low-frequency contents of the WPS become more prominent as large eddies are energized, while the high-frequency contents become less important. Under a favourable pressure

gradient (FPG), however, the opposite applies, with stronger high-frequency contents. The WPS slope in the overlap range also varies with the pressure gradient. Cohen & Gloerfelt (2018) investigated the effects of mild pressure gradient using large-eddy simulations (LES) and showed scale-based dependencies of the WPS on FPG similar to those observed before. Na & Moin (1998) conducted direct numerical simulation (DNS) of a boundary layer with prescribed freestream suction and blowing to induce flow separation and reattachment. They showed that none of the outer, inner or mixed scaling collapsed the wall pressure spectra in all regions of the flow. Normalization with the local maximum magnitude of the Reynolds shear stress, however, was shown to collapse the low-frequency range of WPS for APG flows including those with separation (Abe 2017; Ji & Wang 2012; Caiazzo *et al.* 2023).

Modeling of turbulent WPS is broadly classified in two categories: (i) semi-empirical modelling and (ii) analytical modeling based on solution of the Poisson's equation of pressure (Kraichnan 1956; Panton & Linebarger 1974; Jaiswal *et al.* 2020; Grasso *et al.* 2022; Palani *et al.* 2023; Hales & Ayton 2023). The focus of this paper is on the first approach, which requires a smaller amount of inputs from the flow field in comparison to the analytical modelling approach. Existing semi-empirical WPS closures mostly model the magnitude and shape of the WPS normalized by some boundary-layer parameters that are either internal, external or mixed, such as the boundary layer thickness (δ), the edge velocity (U_e) and the wall shear stress ($\tau_w = \rho u_\tau^2$, where u_τ is the friction velocity), etc. For some of these studies see Kraichnan (1956), Corcos (1964), Willmarth (1975), Amiet (1976), Bull & Thomas (1976), Chase (1980), Goody (2004), Rozenberg *et al.* (2012), Kamruzzaman *et al.* (2015), Lee (2018), Hu (2018), and Pargal *et al.* (2022). One of the most widely used semi-empirical models for ZPG boundary layers was proposed by Goody (2004), which captures accurately the Reynolds number effect on the spectrum for these flows. But for boundary layers under pressure gradients, Goody's model may yield large errors, as shown by a number of studies (Rozenberg *et al.* 2012; Kamruzzaman *et al.* 2015; Catlett *et al.* 2016; Hu *et al.* 2013; Lee 2018; Rossi & Sagaut 2023). For instance, in APG flows the more prominent low-frequency contents and reduced mid-to-high-frequency ones of the WPS were not captured by this model. Rozenberg *et al.*

(2012) integrated additional boundary layer flow parameters to sensitize the model to pressure gradient effects, especially those of APG. The additional parameters include Clauser’s parameter (β) (Clauser 1954) and Cole’s wake parameter (II) (Coles 1956). The former includes the local effect of mean pressure gradients, while the latter represents the cumulative effect of the history of mean pressure gradient up to the considered location in the boundary layer. Several later models developed modifications of the model that capture effects of other complexities such as wall curvature and FPG. Kamruzzaman *et al.* (2015) developed a model by fitting it on a large amount of experimental WPS data collected in various non-equilibrium boundary layer flows on airfoils. Hu (2018) used the shape factor (H) and Reynolds numbers (Re_θ or Re_τ) instead of β to incorporate the effect of non-equilibrium pressure gradients, as β — a descriptor of local pressure gradient — does not carry the history effect of a spatially varying pressure gradient. Lee (2018) improved Rozenberg’s model based on experimental data gathered from a wide range of flows with different Reynolds numbers and pressure gradients. Thomson & Rocha (2022) proposed a new model for flows with FPG. Recently, machine learning approaches such as gene expression programming and artificial neural networks were used to model WPS as a function of boundary layer parameters (Fritsch *et al.* 2022a; Dominique *et al.* 2022; Shubham *et al.* 2023; Ghiglini *et al.* 2023).

Despite the success of the models mentioned above in the specific flows for which they were developed, these models are not universally applicable to both ZPG flows and those with non-equilibrium pressure gradients and/or surface curvature, due to the following reasons. (i) Models developed by curve-fitting to data of a limited type of flows do not naturally apply to other flows, such as Goody’s model, which works for ZPG flows only. (ii) Normalizations of wall pressure statistics used for ZPG flows (e.g. τ_w) may not be appropriate for strong-APG flows (e.g. a boundary layer close to separation where τ_w approaches zero). (iii) Local boundary layer parameters do not account sufficiently for the history effect of the pressure gradient. In addition, some existing models were developed based on experimental wall-pressure measurements that are supplemented with low-fidelity flow-field data, such as those estimated from XFOIL (Drela 1989).

The objective of this study is therefore to develop a general WPS model that is

tunable for both ZPG and non-equilibrium, strong-pressure-gradient turbulent boundary layers, as well as special cases such as flow separation and reattachment. To this end, model parameters that derive from the local mean velocity profile are incorporated to sensitize the model to the streamwise pressure gradient and its history. An appropriate pressure normalization for flows with and without pressure gradients is used. The model is calibrated based on a large and inclusive database, containing both experimental measurements and DNS/LES data (existing or new) of flows over a wide range of Reynolds number, with or without separation.

The organization of the paper is as follows. Section 2 describes the database, Section 3 presents the boundary layer development of the cases in the datasets, Section 4 discusses the wall-pressure fluctuations and WPS in the datasets, Section 5 discusses the performances of existing WPS models and introduces a new generalized WPS model, and conclusions are presented in Section 6.

2. Datasets collection

The first step to develop a generalized WPS model is to collect and analyze high-fidelity datasets in a wide range of flows. The goal is to collect datasets for both equilibrium and non-equilibrium boundary layers, including ZPG, FPG, and APG flows, with or without wall curvature (as in boundary layers developed on airfoils) and boundary layer separation and reattachment, across a wide range of Reynolds number based on momentum thickness ($Re_\theta = 300$ to $23,400$).

2.1. Simulation datasets

DNS and LES datasets are gathered or re-generated from cases in four prior studies: Pargal *et al.* (2022), Wu *et al.* (2019), Na & Moin (1998) and Wu & Piomelli (2018). The first two are DNS cases. Data are collected directly from simulations of turbulent boundary layer on a flat-plate and that on a controlled-diffusion (CD) airfoil with matched non-equilibrium APG distributions along the streamwise direction, as discussed in Pargal *et al.* (2022). The other two studies are DNS and LES studies, respectively, of flat-plate boundary layers with suction and blowing freestream velocities which lead to

boundary layer separation and then reattachment; these two cases are rerun to collect velocity and wall-pressure statistics. For the case of Wu & Piomelli (2018), this work provides new data as the wall pressure was not discussed previously.

Here, the streamwise, wall-normal and spanwise directions are denoted as x , y and z . u , v and w are the velocity components in those directions, t is time, P is the static pressure, ρ is the density and ν is the kinematic viscosity. An instantaneous flow variable $\phi(x, y, z, t)$ is decomposed as $\phi = \bar{\phi}(x, y) + \phi'(x, y, z, t)$, where $\bar{(\cdot)}$ denotes averaging in z and time.

The case of Wu *et al.* (2019) provides DNS data on a boundary layer developing on the pressure side of a CD airfoil. The compressible Navier-Stokes equations are solved with the multi-block structured code HiPSTAR (High Performance Solver for Turbulence and Aeroacoustics Research) (Sandberg 2015). The spatial discretization involves both a five-point fourth-order central standard-difference scheme with Carpenter boundary stencils in the streamwise and crosswise directions (Carpenter *et al.* 1999), and a spectral method using the FFTW3 library in the spanwise direction. The time discretization is achieved by an ultra-low-storage five-step fourth-order Runge-Kutta scheme (Kennedy *et al.* 1999). Characteristic-based boundary conditions are used to prevent spurious reflections at the computational domain boundaries (Sandberg & Sandham 2006; Jones *et al.* 2008). Details of the problem formulation are provided by Wu *et al.* (2019).

The case of Pargal *et al.* (2022) is an incompressible DNS of a flat-plate turbulent boundary layer to emulate the boundary layer development on the downstream portion of the CD airfoil flow studied by Wu *et al.* (2019). A finite difference solver on a staggered grid was used. It employs second-order, central differences for all spatial derivatives and second-order Adams-Bashforth semi-implicit time advancement. To match the pressure gradient parameter (K) of the airfoil boundary layer, a streamwise pressure gradient is imposed by prescribing a streamwise-varying $U_\infty(x)$ at the top boundary of the domain. The wall-normal freestream velocity $V_\infty(x)$ is then obtained based on the conservation of mass. A fully turbulent boundary layer flow at the inlet of the domain is obtained using the recycling/rescaling method (Lund *et al.* 1998). A convective outflow boundary condition (Orlanski 1976) is used at the outlet and periodic boundary conditions are used

in the spanwise direction. Similar discretization methods and boundary conditions were used in Wu & Piomelli (2018) and Na & Moin (1998) with slight variations in details. Simulations of the flows in these two studies were rerun, based on the methodologies of Pargal *et al.* (2022). For the LES case of Wu & Piomelli (2018), the governing equations were solved for the filtered quantities. The sub-grid stress tensor was modeled using a dynamic eddy-viscosity model (Germano *et al.* 1991; Lilly 1992), in which the coefficient was adjusted using the Lagrangian-Averaging procedure (Meneveau *et al.* 1996). Boundary layer developments in the rerun simulations will be compared to those reported in the original studies in Section 3.

2.2. Experimental datasets

DNS and LES simulations are limited to comparatively low Reynolds numbers. Experimental datasets are gathered from the studies of Hu & Herr (2016), Fritsch *et al.* (2022*b*), and Goody (2004), which provide ZPG or pressure gradient flow data with Re_θ of up to 23,400. A brief description of the experimental setup of each case is given below. Hu (2018) carried out experiments in an open-jet anechoic test section of Acoustic Wind Tunnel Braunschweig (AWB). Adverse and favorable pressure gradients in flat-plate boundary layers were achieved by placing a rotatable NACA 0012 airfoil above the flat plate. Wall-pressure statistics were measured with sub-miniature pressure transducers and boundary layer velocity profiles were obtained using hot wires. Re_θ was up to 19,000, with $\beta = -0.9$ to 16. The study is among the few experimental studies that measured wall-pressure statistics across very different flows due to the very wide ranges of pressure gradient and Reynolds number. Similarly, Fritsch *et al.* (2022*b*) carried out experiments in a subsonic wind tunnel with a NACA 0012 airfoil installed in the center of the test section. The boundary layer was tripped at the upstream section, to ensure a fully turbulent boundary layer in the test section. Wall-pressure statistics were measured for non-equilibrium pressure gradients ranging from β of -0.5 to 0.5 , with Re_θ reaching 18,000. Goody & Simpson (2000) carried out measurements in the boundary-layer tunnel of the Aerospace and Ocean Engineering department of Virginia Tech. The wall-pressure statistics measurement was limited to ZPG flows but data reached Reynolds numbers as

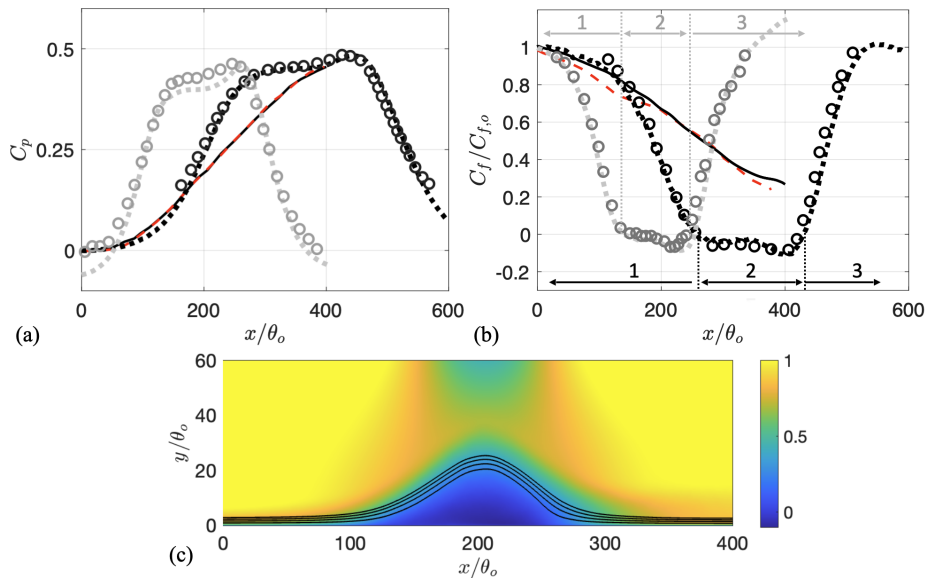


FIGURE 1. Streamwise development of pressure coefficient (a) and friction coefficient (b) in the simulated cases: — Pargal *et al.* (2022), -- Wu *et al.* (2019), --- Wu & Piomelli (2018), and --- Na & Moin (1998), compared to original data of Wu & Piomelli (2018) and Na & Moin (1998) (o). (c) Contour of mean streamwise velocity normalized by U_o in Wu & Piomelli (2018) case, with streamlines shown at stream-function values of $\psi_o = 0.5, 1, 1.5$ and 2.

high as $Re_\theta = 23,400$.

3. Boundary layer development

In this section, the streamwise developments of pertinent flow and boundary layer variables are presented for cases in the database. The goal is to provide insights on the appropriate choice of scaling variables for WPS modeling in non-equilibrium flows.

Figure 1 shows the variation of the mean wall-pressure coefficient, $C_p = (p|_{y=0} - p_e)/(0.5\rho U_e^2)$, and skin friction coefficient, $C_f = (u_\tau/U_e)^2/2$, where p_e is edge static pressure at the location of $x = 0$, which corresponds to the reference (ZPG) location defined in each of the studies. In Figure 1(b), the C_f is normalized by its value at the reference location to better compare all cases. Only simulated cases are presented as the boundary parameters for a continuous range of x are available. Figures 1(a) shows that the variations of C_p in the flat-plate (Pargal *et al.* 2022) and airfoil (Wu *et al.* 2019) cases are matched, as required by the flat-plate case setup; comparison between these two flows reveal the effects of convex wall curvature on WPS. In Figures 1(b), the variations

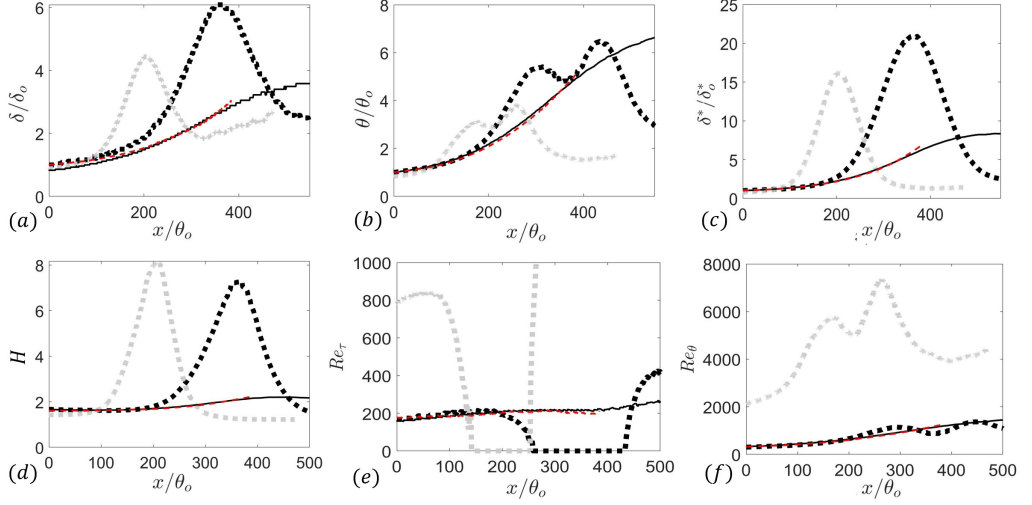


FIGURE 2. Development of boundary layer parameters in the simulated cases. For legend see Figure 1.

of C_f are shown to match overall for these two cases, with some differences near the airfoil trailing edge due to the convex wall curvature and trailing-edge effects. These comparisons are discussed in Pargal *et al.* (2022). In the cases of Na & Moin (1998) and Wu & Piomelli (2018) where the flows undergo freestream suction and blowing, the C_p variation indicates three phases of a separated boundary layer flow (marked in Figures 1(b)): (1) attached APG flow, (2) separated region and (3) reattached flow under FPG. This is also reflected in C_f variations: C_f first decreases toward zero in the APG region, reaching negative values in the separated flow region, and increases near the flow reattachment in the FPG region. The contour of mean streamwise velocity of the case of Wu & Piomelli (2018) in Figure 1(c) confirms these flow stages. The coefficients are compared between the results of the present rerun simulations and those of the original studies (Na & Moin 1998; Wu & Piomelli 2018); good match is obtained in both cases.

In Figure 2, the variations of boundary layer thickness (δ), momentum thickness (θ) and displacement thickness (δ^*) along the streamwise direction are shown. As expected with an increase in APG, the boundary layer becomes thicker. For the cases with suction and blowing, the thicknesses reach their maxima near the end of the APG zone and then decrease with FPG. The development of the shape factor, H , in Figure 2(d) shows a similar response, which reflects that the displacement thickness is more sensitive to the

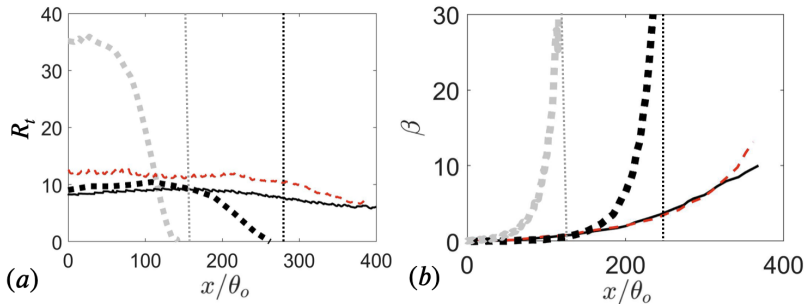


FIGURE 3. Development of R_t and β in the simulated cases. For legend see Figure 1. For Wu & Piomelli (2018) and Na & Moin (1998) cases, only the attached-flow region upstream of the separation point is shown; --- (vertical): location of separation point.

pressure gradients compared to the momentum thickness.

Reynolds numbers based on different velocity scales are compared. The one based on the inner velocity, $Re_\tau = u_\tau \delta / \nu$, shows a similar trend as that of C_f (Figure 2(e)), while the one based on edge velocity, $Re_\theta = U_e \theta / \nu$, shows a variation similar to that of θ (Figure 2(f)). The DNS cases are conducted in low Reynolds numbers ($Re_\theta \approx 300$ to 1200), while higher values are reached for the LES case ($Re_\theta \approx 2000$ to 7000).

Figure 3 shows the streamwise developments of two boundary layer parameters that are used in most existing WPS models to sensitize the modeled spectrum to the Reynolds number and the pressure gradient: $R_t \equiv Re_\tau (u_\tau / U_e)$ (Figure 3 (a)) and β (Figure 3 (b)), respectively. As the separation point is approached, R_t tends to 0 and β to infinity. This indicates issues in many existing WPS models when used for strong-APG flows near incipient separation (Caiazzo *et al.* 2023), which are examined in detail in Section 5.1.

For most of the experimental datasets, streamwise variations of the boundary layer parameters are available at discrete locations only. Representative values of Re_θ , H , C_f and β are tabulated in Table 1. Specifically, the datasets of Hu (2018) experiments contain five cases: one ZPG flow, three APG flows with β varying from 4 to 12, and one FPG flow, at $Re_\theta = 5,000$ to 11,000. The data show that boundary layer thicknesses (as indicated here by Re_θ ; for other thicknesses see the original studies) and the shape factor increase with APG and decrease in FPG, whereas C_f decreases with APG and increases in FPG. The cases from Fritsch *et al.* (2022b) are non-equilibrium APG and FPG flows but with comparatively milder APG compared to Hu (2018). As a result, the variations in boundary layer parameters are more limited. Also included are measurements by

Cases	Re_θ	H	C_f	β
Hu (2018), ZPG	4889	1.41	0.0025	0
Hu (2018), APG (-6°)	6979	1.61	0.0017	3.8
Hu (2018), APG (-10°)	8670	1.75	0.0012	6
Hu (2018), APG (-14°)	11046	2.12	0.0006	12.5
Hu (2018), FPG (14°)	1940	1.26	0.0068	-0.5
Fritsch <i>et al.</i> (2022b), ZPG (2°)	16000	1.29	0.0026	-0.02
Fritsch <i>et al.</i> (2022b), APG (12°)	18606	1.31	0.0024	0.58
Fritsch <i>et al.</i> (2022b), FPG (-10°)	14000	1.26	0.0028	-0.47
Goody & Simpson (2000), ZPG	7300	1.29	0.0026	0
Goody & Simpson (2000), ZPG	23400	1.29	0.0022	0

TABLE 1. List of experimental datasets and values of boundary layer parameters at measurement locations of available data. For Hu (2018) and Fritsch *et al.* (2022b) datasets, the angle of attack of the airfoil imposed to generate mean pressure gradient is indicated.

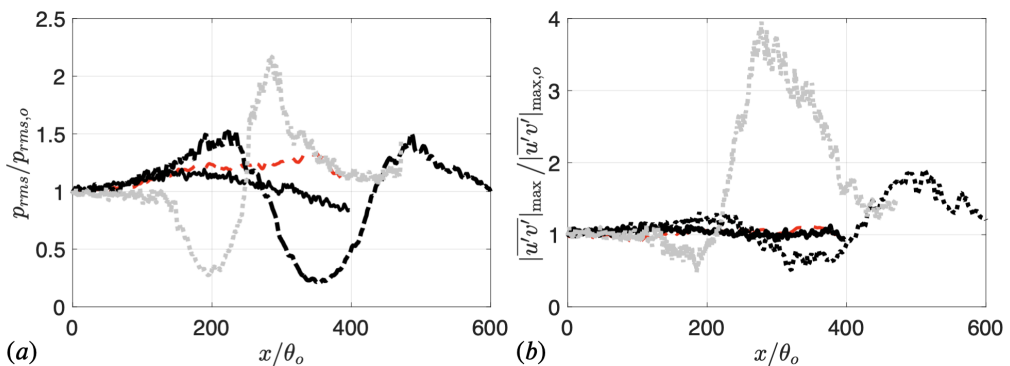


FIGURE 4. (a) Streamwise variation of the wall-pressure r.m.s, normalized by its value at the reference location. (b) Streamwise variation of the local peak magnitude of Reynolds shear stress, normalized by its value at the reference location. For legend see Figure 1.

Goody & Simpson (2000), which were carried out for ZPG flows only but reached higher Reynolds numbers.

4. Wall-pressure statistics

In this section, the development of wall-pressure statistics along x is discussed using the datasets. Different normalizations are used to analyze the wall-pressure scaling. Effects of pressure gradient, boundary layer separation and reattachment on the wall-pressure spectrum are examined.

For the simulation datasets, streamwise variations of the root-mean-square (r.m.s.) of

wall-pressure fluctuations, normalized by their specific values at $x = 0$, are compared in Figure 4(a). Convex wall curvature and trailing edge effect intensify the wall pressure fluctuations, as shown by the comparison between the flat-plate case of Pargal *et al.* (2022) and the airfoil case of Wu *et al.* (2019) for $x/\theta_o > 200$. In the separated-flow region, a drop in wall-pressure fluctuations is seen, which was also observed by Abe (2017). The dip is attributed to the departure of turbulent eddies from the wall, with mainly large recirculating eddies interacting with the near-wall region. As the separated shear layer reattaches, the re-emergence of intense turbulent motions near the wall leads to an augmentation of wall-pressure fluctuations, shown by the $p_{rms}(x)$ maximum shortly after the reattachment point (at $x/\theta_o \approx 280$ for Wu & Piomelli (2018) and $x/\theta_o \approx 500$ for Na & Moin (1998)). Interestingly, Figure 4(b) shows that the x variation of the local maximum magnitude of the Reynolds shear stress profile, $|\overline{u'v'}|_{\max}(x)$, is very similar to that of p_{rms} : the decrease near the separation point and the peak near the flow reattachment occur at almost the same x locations. Downstream from the reattachment point, as the flow recovers towards the equilibrium ZPG flow, both p_{rms} and $|\overline{u'v'}|_{\max}$ reduce towards the ZPG values at $x = 0$.

In Figure 5 different quantities are used to normalize wall-pressure r.m.s. as it varies along x . The r.m.s. normalized by τ_w (Figure 5(a)) increases with APG and tends towards infinity as the separating point is approached. The use of τ_w to scale p_{rms} in WPS models is, therefore, inappropriate for strong-APG boundary layers. The r.m.s. normalized by $q_e = 0.5 \rho U_e^2$ (Figure 5(b)) displays a significant increase in the APG zone before the flow separation. This is because wall-pressure fluctuations are augmented in the APG region, while the edge velocity decreases. In comparison, $p_{rms}/(\rho |\overline{u'v'}|_{\max})$ stays almost constant as long as the boundary layer is attached, regardless of the pressure gradient (Figure 5(c)). In the separated flow regions, however, a dip of $p_{rms}/(\rho |\overline{u'v'}|_{\max})$ is observed, caused by a faster damping of p_{rms} inside the recirculation bubble than that of the Reynolds shear stress in the detached shear layer (as shown in Figure 4). These observations indicate that wall-pressure r.m.s. scales better with $\rho |\overline{u'v'}|_{\max}$ than with q_e or τ_w , in attached flows under strong pressure gradients; similar observations were made by Na & Moin (1998), Abe (2017) and Caiazzo *et al.* (2023). However, the appropriate wall-pressure

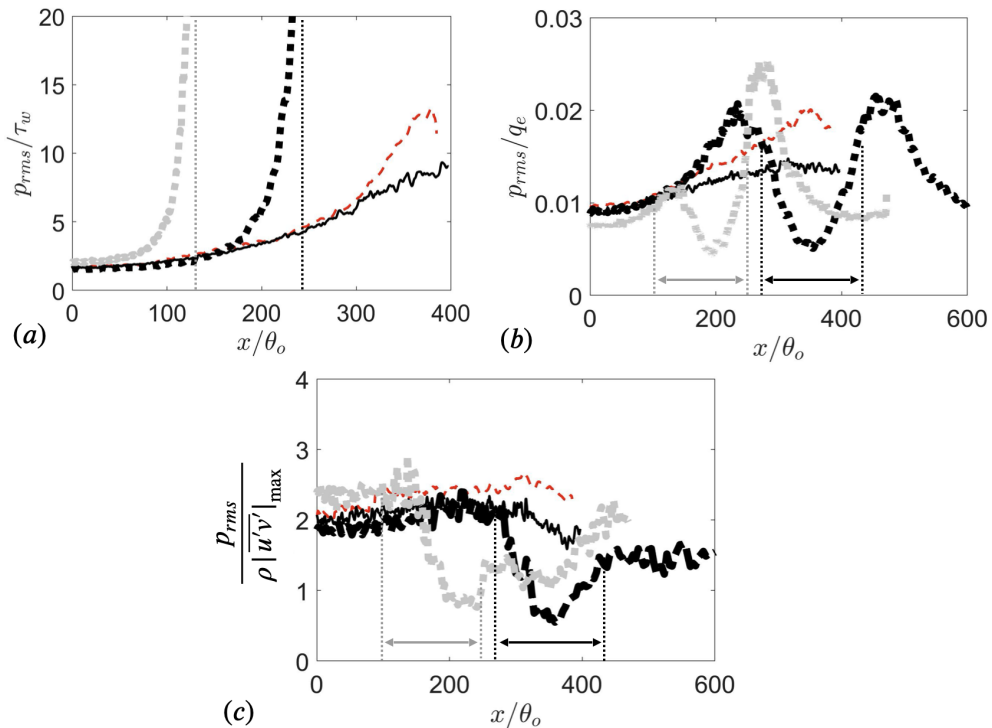


FIGURE 5. Wall-pressure r.m.s. variation normalized by (a) local wall shear stress (τ_w), (b) local dynamic pressure (q_e), and (c) local peak magnitude of Reynolds shear stress. In (a), --- (vertical): locations of separation points. In (b) and (c), separated-flow regions are marked. For legend see Figure 1.

r.m.s. scaling for the separated flow region remains yet to be found; but this is out of the scope of the present work.

The PSD of the wall-pressure fluctuations (denoted by ϕ_{pp}) is computed for all simulated and experimental cases and compared in Figure 6. Only attached-flow regions, with ZPG or non-equilibrium APG, are considered here. The x location, β value, and legend for each PSD curve in Figure 6 are listed in Table 2. Different normalizations are compared. Both Re_θ ($Re_\theta = 300$ to $23,400$) and β ($\beta = 0$ to 200) vary greatly among these data. The high β values occur near the separation points.

Figure 6(a) compares the results using $-\rho|\overline{u'v'}|_{\max}$ as the pressure scale, δ the length scale, and U_e the velocity scale (or equivalently p_{rms} , δ^* and the Zagarola-Smits velocity, as shown by Caiazzo *et al.* (2023)). Note that in the experimental datasets the Reynolds shear stress data were missing. For these cases, the wall shear stress (τ_w) at a mild-APG ($\beta < 1$) location immediately upstream of the APG region, instead of the local

Cases	Legend
Pargal <i>et al.</i> (2022), $x/\theta_o = 0$, ZPG ($\beta = 0$)	—
Pargal <i>et al.</i> (2022), $x/\theta_o = 100$, Low APG ($\beta = 0.3$)	—
Pargal <i>et al.</i> (2022), $x/\theta_o = 290$, APG ($\beta = 5$)	—
Pargal <i>et al.</i> (2022), $x/\theta_o = 340$, High APG ($\beta = 8$)	—
Wu <i>et al.</i> (2019), $x/\theta_o = 0$, ZPG ($\beta = 0.01$)	---
Wu <i>et al.</i> (2019), $x/\theta_o = 100$, Low APG ($\beta = 0.28$)	---
Wu <i>et al.</i> (2019), $x/\theta_o = 290$, APG ($\beta = 4.8$)	---
Wu <i>et al.</i> (2019), $x/\theta_o = 340$, High APG ($\beta = 8.3$)	---
Wu & Piomelli (2018), $x/\theta_o = 50$, Low APG ($\beta = 0.9$)	—
Wu & Piomelli (2018), $x/\theta_o = 105$, Very high APG ($\beta = 22.8$)	—
Wu & Piomelli (2018), $x/\theta_o = 120$, Very high APG ($\beta = 46.28$)	—
Wu & Piomelli (2018), $x/\theta_o = 130$, Before flow separation ($\beta = 171$)	—
Na & Moin (1998), $x/\theta_o = 50$, ZPG ($\beta = 0.018$)	—
Na & Moin (1998), $x/\theta_o = 210$, High APG ($\beta = 8$)	—
Na & Moin (1998), $x/\theta_o = 230$, Before flow separation ($\beta = 162$)	—
Hu (2018), ZPG ($\beta = 0.1$)	●
Hu (2018), High APG (-10°) ($\beta = 6$)	●
Hu (2018), Very high APG (-14°) ($\beta = 12.5$)	○
Hu (2018), FPG (14°) ($\beta = -0.5$)	○
Fritsch <i>et al.</i> (2022b), ZPG (2°) ($\beta = 0$)
Fritsch <i>et al.</i> (2022b), APG (12°) ($\beta = 0.5$)
Fritsch <i>et al.</i> (2022b), FPG (-10°) ($\beta = -0.5$)
Goody & Simpson (2000), ZPG (7300) ($\beta = 0$)
Goody & Simpson (2000), ZPG (23400) ($\beta = 0$)

TABLE 2. Datasets in attached-flow regions (under ZPG or APG) that are considered in analyses of wall-pressure spectrum.

Reynolds shear stress, is used to form the pressure scale for the strong-APG region. This approximation is based on the observation that $|\overline{u'v'}|_{\max}(x)$ does not vary significantly in the attached-flow region upstream of the separation point (Figure 4(b)). The value of $|\overline{u'v'}|_{\max}(x) \approx |\overline{u'v'}|_{\max}(0)$ can then be approximated as $\tau_w(0)$ due to the existence of a constant-stress layer in a boundary layer under zero or mild pressure gradients. The treatment mentioned above is employed for the experimental cases only. Under such normalization, Figure 6(a) shows that approximate low-frequency collapse is obtained. This is expected as the low-frequency contents are the main contributor to p_{rms} , which in turn scales with $\rho|\overline{u'v'}|_{\max}$. Swapping the length scale for δ^* or θ , however, gives more scatter in the low-frequency range (Figures 6(b) and (c)), as also shown by Caiazzo *et al.*

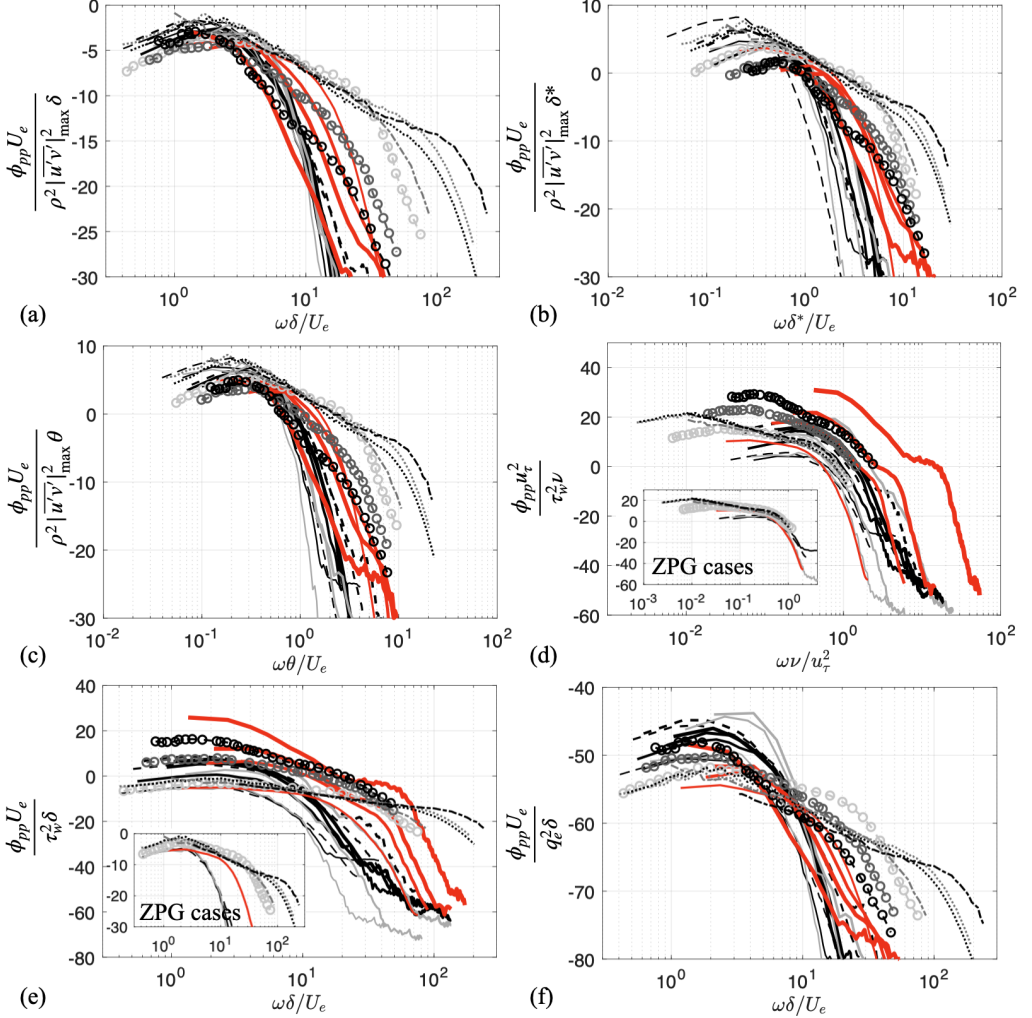


FIGURE 6. Power spectral density (PSD) of wall-pressure fluctuations for attached-flow datasets with ZPG and APGs listed in Table 2, normalized by three different scalings involving $\rho|u'v'|_{\max}$ (as the pressure scaling) and outer scales: (a) $\rho|u'v'|_{\max}$, δ and U_e , (b) $\rho|u'v'|_{\max}$, δ^* and U_e and (c) $\rho|u'v'|_{\max}$, θ and U_e . Normalizations with (d) inner scales (τ_w , δ_ν and u_τ), (e) mixed scales (τ_w , δ and U_e), and (f) outer scales (q_e , δ and U_e). The PSD is evaluated in dB. Insets show ZPG profiles, demonstrating high-frequency collapse in (d) and low-frequency collapse in (e), respectively. Legend is listed in Table 2.

(2023). Even though previous works (Kamruzzaman *et al.* 2015; Abe 2017; Caiazzo *et al.* 2023) have shown $\rho|u'v'|_{\max}$ to be the best pressure scaling for wall-pressure spectra, most of them were limited to low Reynolds number cases with mild pressure gradients. Here, the chosen set of scaling is shown to collapse low-frequency portion of the PSD for a large range of Reynolds number with strong non-equilibrium APG also.

In comparison, normalization based on inner velocity and length scale only (i.e. using

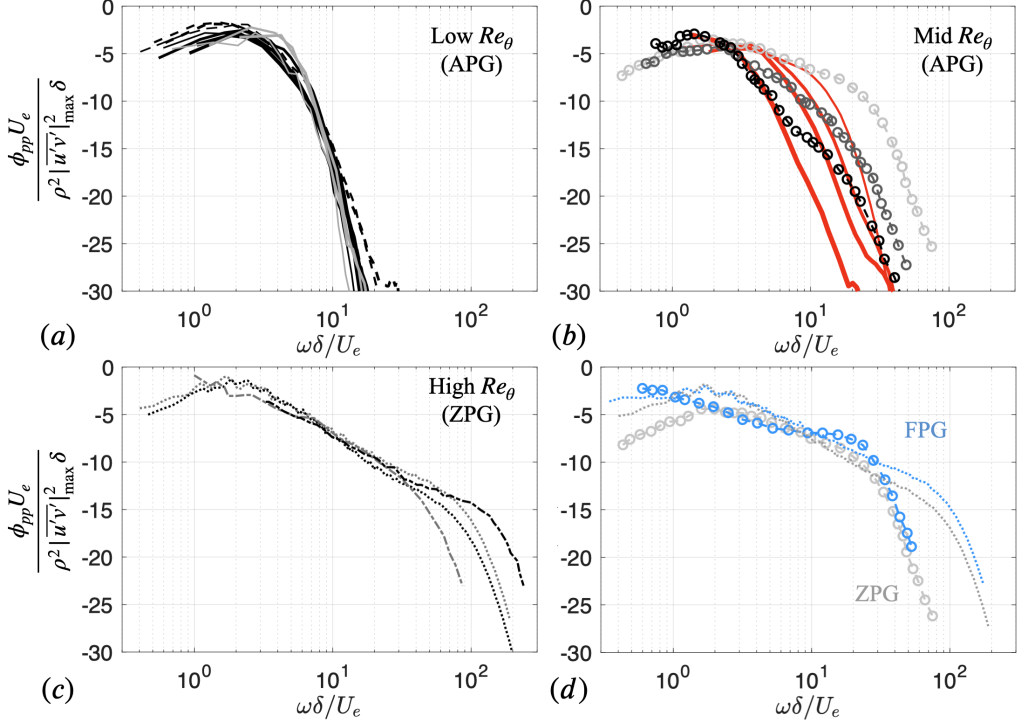


FIGURE 7. Wall-pressure PSDs in APG boundary layers with different Reynolds number ranges: (a) low- Re_θ range ($Re_\theta = 300$ to 1000), (b) mid- Re_θ range ($Re_\theta = 2000$ to 8000), and (c) high- Re_θ range ($Re_\theta = 8000$ to $23,400$). (d) PSDs in FPG flows (blue) compared to ZPG ones (gray). See Table 2 for legend.

τ_w , $\delta_\nu \equiv \nu/u_\tau$ and u_τ as shown in Figure 6(d)) gives a high-frequency collapse for the ZPG spectra, but a large scatter for the APG ones. When mixed variables are used (i.e. using τ_w , δ and U_e as shown in Figure 6(e)), which is commonly applied in existing WPS models, the low-frequency range collapses for the ZPG spectra only, but not for cases with strong APG, as p_{rms} does not scale with τ_w . On the other hand, normalization based on outer variables only (i.e. using q_e , δ and U_e as shown in Figure 6(f)) gives a better collapse than that based purely on the inner variables; however, it still fails to collapse the low-frequency range. Based on these observations, the best ϕ_{pp} scaling among these options is thus $(\rho|\overline{u'v'}|_{\max})^2 \delta / U_e$.

The effects of Reynolds number are analyzed next. Figures 7(a-c) categorize the wall pressure PSDs in APG and ZPG flows into three Reynolds number groups: low- Re_θ ($Re_\theta \approx 300$ to 1000), mid- Re_θ ($Re_\theta \approx 200$ to $8,000$) and high- Re_θ ($Re_\theta \approx 8,000$ to $23,400$) groups. Note that in the high- Re_θ group, only ZPG or mild-APG flows are

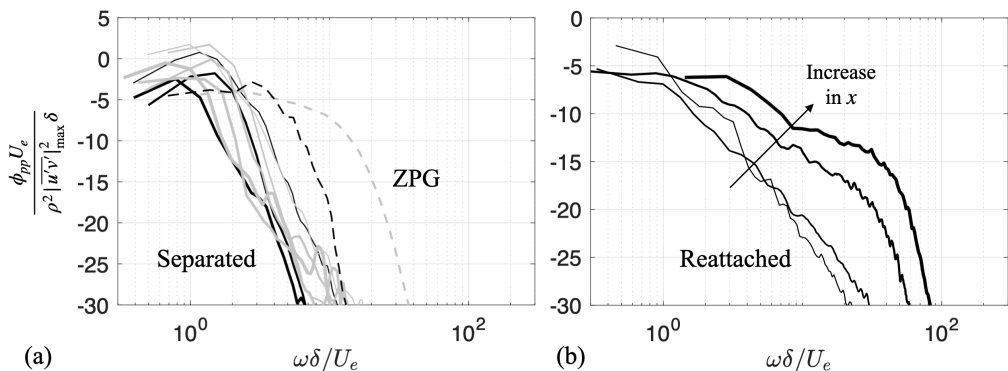


FIGURE 8. (a) Wall-pressure PSDs in separated-flow regions (—) compared to those at respective reference ZPG locations (---); gray lines show Wu & Piomelli (2018) data at $x/\theta_o = 150, 175, 200, 220$ and 240 ; black lines show Na & Moin (1998) data at $x/\theta_o = 270, 300$ and 400 . (b) Wall-pressure PSDs in reattached-flow region of Wu & Piomelli (2018), at $x/\theta_o = 275, 300, 350$ and 450 . Increase in line thickness indicates downstream direction.

available in the present datasets. Figure 7(a) shows that all low- Re_θ spectra collapse very well in the majority of frequency range. This is because the overlap range is limited and the low-frequency range is well collapsed by using $\rho|\overline{u'v'}|_{\max}$ as the pressure scaling. At higher Reynolds numbers, the overlap range appears and grows with Re_θ (Figures 7(b,c)). The width of the overlap range is shown to decrease with APG and the slope of this range increases with APG.

The PSDs in FPG flows are shown in Figure 7(d) using the two FPG datasets (in blue) of Hu (2018) and Fritsch *et al.* (2022b), as compared to the corresponding ZPG spectra (in gray) from these two studies. Under $\beta \approx -0.5$ (relatively mild FPG), both spectra show a milder slope in the overlap range than the ZPG PSDs. This is consistent with the increase in slope for APG flows discussed above. In addition, the overlap ranges are slightly widened under FPG with the low-frequency limit moving towards lower frequencies, especially for the lower-Reynolds-number case (Hu 2018). This is associated with a weaker mean-flow wake region under FPG.

To analyze the WPS associated with separated and reattached flows, Figures 8(a) and 8(b) compare the spectra extracted, respectively, from the separated-flow regions and the regions downstream of the boundary layer reattachment in the cases of Na & Moin (1998) and Wu & Piomelli (2018). Figures 8(a) shows that in the separated-flow regions both overlap-range and high-frequency wall-pressure fluctuations are reduced compared

Model	Legend
Goody (2004)	—
Lee (2018)	---
Rozenberg <i>et al.</i> (2012)	----
Hu (2018)	---
Kamruzzaman <i>et al.</i> (2015)	----
Proposed model	—

TABLE 3. List of WPS models examined with the present datasets.

to those in respective reference ZPG locations (dashed lines), due to the departure of intense turbulent motions from the wall following the detachment of the shear layer. The scaling does not collapse the low-frequency range as it does for attached flows. This is expected as the wall pressure r.m.s does not scale with $|\overline{u'v'}|_{\max}$ in this region (Figures 5(c)). However, it is interesting that the shape of the spectrum does not vary significantly in the separated-flow region: the spectra in Figures 8(a) all display a narrow low-frequency peak with greatly reduced high-frequency contribution. Downstream from the reattachment point, Figure 8(b) shows that the spectrum recovers gradually from the low-frequency-dominant state inside the separated-flow region towards the equilibrium state, with augmented mid- to high-frequency contents.

5. Wall-pressure spectra modelling

5.1. Performance of existing wall-pressure spectra models

Most existing wall-pressure spectral models are developed for regions with zero and adverse pressure gradients. Figure 9 compares a number of existing WPS models introduced in Section 1 against the present datasets of ZPG and APG (attached regions only) flows (marked by blue solid lines) for a few Re_θ - β combinations. Among them, Figures 9(d,e) show two examples near boundary-layer separation. The models and their legend are listed in Table 3. The optimal ϕ_{pp} normalization as identified in Section 4 is used. Results of the new generalized model (shown by red solid lines) to be introduced in Section 5.2 is also compared. The comparison demonstrates dependencies of the WPS on the APG and the Reynolds number as discussed in Section 4. Under the present normalization, the main variations are in the width and slope of the overlap range.

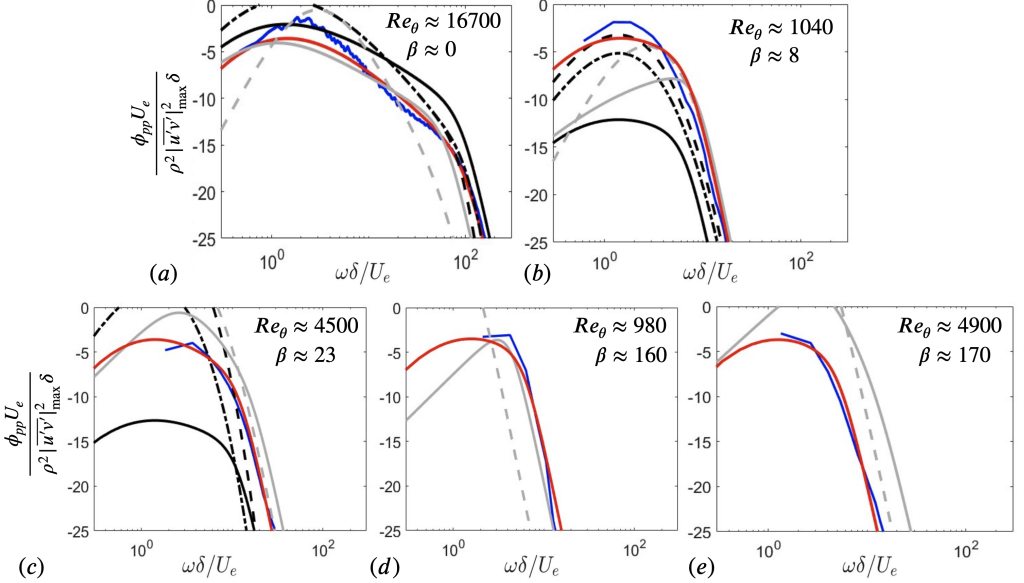


FIGURE 9. Comparison between predictions of WPS models and numerical or experimental measurements (—), for different types of flow: (a) weak-APG and high-Reynolds-number flow (Fritsch *et al.* 2022b, 12°), (b) strong-APG and low-Reynolds-number flow (Wu *et al.* 2019), (c) very-strong-APG flow at intermediate Reynolds number (Wu & Piomelli 2018), (d) flow near separation point at a low Reynolds number (Na & Moin 1998), and (e) flow near separation point at an intermediate Reynolds number (Wu & Piomelli 2018). All models predictions are re-normalized in chosen scaling for comparison purposes. Legend of model results is given in Table 3.

In the (almost) ZPG region (Figure 9 (a)), all tested models are shown to give reasonably good overall predictions. Kamruzzaman *et al.* (2015) model does not produce an overlap range and, as a result, yields significantly under-predicted high-frequency contents. Moreover, except for Hu (2018) model, all existing models over-predict the spectrum in the overlap range, partially because of a mismatch in the slope.

For a flow under relatively weak APG ($\beta \approx 8$), Figure 9(b) shows that Rozenberg *et al.* (2012) and Lee (2018) models give very good overall predictions, whereas Hu (2018) and Kamruzzaman *et al.* (2015) models under-predict the WPS at low frequencies. Goody (2004) model under-predicts the WPS in the whole frequency range, which is expected, as this model was developed and calibrated for ZPG flows only.

In strong-APG flows (Figure 9(c-e)), especially near the boundary layer separation point, the existing models give large errors. This is because the model parameters used in these models: R_t and β , tend towards zero and infinity, respectively. Another source of error is the inappropriate pressure scaling (i.e. τ_w) used in the models. For instance,

Rozenberg *et al.* (2012) model:

$$\frac{\phi_{pp}(\omega)U_e}{\tau_w^2\delta^*} = \frac{0.78(1.8\Pi\beta + 6)(\omega\delta^*/U_e)^2}{[(\omega\delta^*/U_e)^{0.75} + C'_1]^{3.7} + [C'_3(\omega\delta^*/U_e)]^7}, \quad (5.1)$$

where $C'_3 = 3.76R_T^{-0.57}$, reaches a singularity as τ_w and R_t become zeros and β becomes infinity. This issue is common in existing models. In addition, most of these models were fitted to limited types of flows, such as low-Reynolds-number airfoil boundary layers in Kamruzzaman *et al.* (2015), flat-plate boundary layers in Hu (2018), and ZPG flows in Goody (2004). Moreover, sometimes the boundary layer flow properties used for model calibration were estimated from lower-fidelity methods such as XFOIL or RANS calculations. Employing τ_w as the pressure scale for ϕ_{pp} also renders the dimensionless spectrum complicated to model, even for attached flows at strong APGs, as the dimensionless ϕ_{pp} displays large variations. In Section 5.2, these limitations are addressed to develop a well-behaved WPS model for both ZPG and APG flows, which can be attached or separated.

5.2. A new generalized WPS model for non-equilibrium boundary layers

Goody (2004) model is modified by replacing the Reynolds number and pressure gradient parameters with new model inputs that derive directly from the local mean velocity distribution, $U(x, y)$, and are not defined based on u_τ . Only inputs that are quantifiable from engineering predictive approaches (such as RANS models) are considered, so the model is of practical use in engineering applications. The dependence of these inputs on the $U(y)$ distribution at a given x location allows the model to sense the local state of the turbulent boundary layer.

Goody (2004) model reads

$$\tilde{\phi}_{pp}(\tilde{\omega}) = \frac{a\tilde{\omega}^b}{(h\tilde{\omega}^c + d)^e + (f\mathcal{F}\tilde{\omega})^g}, \quad (5.2)$$

where $\tilde{\phi}_{pp} = \phi_{pp}/\phi_{pp}^*$ and $\tilde{\omega} = \omega/\omega^*$ are dimensionless WPS and frequency, respectively, based on a spectrum scaling of ϕ_{pp}^* and a frequency scaling of ω^* as listed in Table 4. The coefficients a to h and the function \mathcal{F} are defined in Table 4. The model was developed based on the observed dependencies of the low-frequency spectrum on the outer scales,

Parameters in Equation (5.2)	Goody (2004)	Present model
ϕ_{pp}^*	$U_e/(\tau_w^2 \delta)$	$U_e/[(\rho \overline{u'v'} _{\max})^2 \delta]$
ω^*	δ/U_e	δ/U_e
a	3	3
b	2	2
c	0.75	$\min[1, 0.8 + (3.34e^{-4})II^{1.86}(y_w^+)^{0.76}]$
d	0.5	0.7
e	3.7	3.7
f	1.1	1
g	7	7
h	1	1
\mathcal{F}	$R_t^{-0.57}$	$(y_w^+)^{-0.37}$
Separated flow ($\tau_w \leq 0$)	-	$y_w^+ = 2, c = 0.75, d = 0.5$
Limited-log-layer flow ($y_w^+ < 15$)	-	$y_w^+ = 15, c = 0.85$

TABLE 4. Comparison between Goody (2004) model and the proposed model. ϕ_{pp}^* and ω^* are the chosen scalings for WPS and frequency, respectively. Special treatments for flow region characterized by a separated boundary layer or a limited logarithmic layer are listed.

as well as that of the high-frequency spectrum on the inner scales, in a ZPG or weak-pressure-gradient flow. The model was known to predict well the overlap range of the spectrum for ZPG boundary layers (as also shown in Figure 9(a)), which depends on the Reynolds number only. The dependence is captured by including R_t in the model. However, the overlap-range spectrum also depends on the pressure gradient in strong-pressure-gradient boundary layers. In Figure 10(a), the prediction of the original Goody's model is examined at several x locations of the Wu & Piomelli (2018) case in the attached-flow region with weak to strong APGs. In this region, β ranges from 0 to 200 and Re_θ is from 2000 to 6000. With the increase in APG, Goody's model shows increasing under-prediction in the whole frequency range.

In the following, the main model changes (as listed in Table 4) are introduced and progressively applied to demonstrate the improvement of each change. First, the pressure scale (i.e. τ_w) on the left-hand-side of Equation (5.2) is replaced with $\rho|\overline{u'v'}|_{\max}$, with the additional change of replacing the constant $d = 0.5$ with 0.7 for a better low-frequency collapse with current data. The effect of these modifications is shown in Figure 10(b), where the low-frequency range is shown accurately predicted for all the x locations. The use of $\rho|\overline{u'v'}|_{\max}$ ensures that the spectral values are finite near the separation point.

Next, to capture the variation of overlap and high-frequency range in APG flows, a

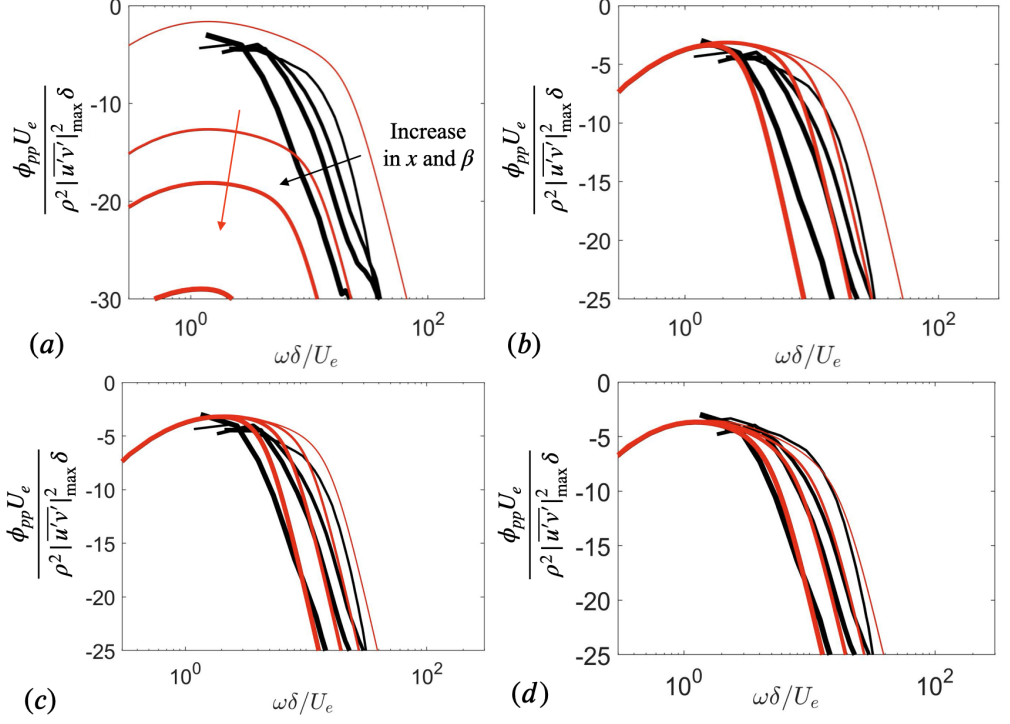


FIGURE 10. Comparison between model predictions of Equation (5.2) with progressive changes described in text (—) and Wu & Piomelli (2018) (—) data in the attached-flow region with weak to strong APGs, to show improvement brought by each model change. (a) Goody (2004) model, (b) pressure scaling changed from τ_w to $\rho |\overline{u'v'}|_{\max}$, (c) additionally replacing dependence on Re_t with that on y_w^+ , (d) further addition of Coles' parameter. Thicker lines indicate increase in x (corresponding to increasing β).

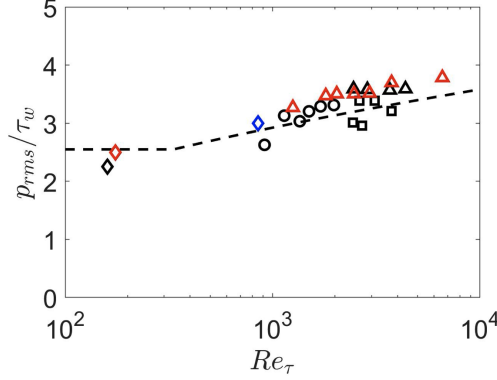


FIGURE 11. Variation of wall-pressure r.m.s. normalized by τ_w in ZPG flows: \diamond Wu *et al.* (2019), \diamond Pargal *et al.* (2022), \diamond Wu & Piomelli (2018), \triangle Blake (1970), \triangle Simpson *et al.* (1987), \circ Farabee & Casarella (1991) and \square Bull & Thomas (1976). --- $p_{rms}^2/\tau_w^2 = 6.5$ for $Re_\tau < 333$ and $p_{rms}^2/\tau_w^2 = 6.5 + 1.86 \ln(Re_\tau/333)$ for $Re_\tau \ge 333$ (Farabee & Casarella 1991).

new parameter is needed to replace R_t to model the width change of the overlap range. Turbulent fluctuations in the logarithmic layer are known as the main contributor to the overlap range of the WPS. For example, Farabee & Casarella (1991) showed that for ZPG boundary layers, with an increase in Reynolds number accompanied by a thickening of the logarithmic layer, the overlap range becomes wider and p_{rms}/τ_w increases. This dependency is also shown by the current ZPG datasets in Figure 11. Additional evidence is provided by Jaiswal *et al.* (2020), who showed that the logarithmic layer yields the highest contribution to the overlap range of ϕ_{pp} based on analyses of the velocity sources of wall-pressure Poisson’s equation. Here, a new model input is introduced: $y_w^+(x)$, defined as the local elevation of the upper edge of the logarithmic layer, to sensitize the model spectrum to the change in logarithmic layer thickness due to Reynolds number and/or pressure gradients. Specifically, the term $1.1R_t^{-0.57}$ is replaced with $(y_w^+)^{-0.37}$, with the constant fitted from present data.

The parameter $y_w^+(x)$ is dynamically determined based on the boundary layer mean velocity $U(x, y) = \bar{u}$, as the y^+ location where $U^+(x, y) - [\kappa(x)^{-1} \log y^+ + B(x)]$ departs from 0 at the upper limit of the logarithmic layer (as shown in Figure 12(c)). Here, κ is the von Kármán constant and B is the log-law intercept, both of which allowed to vary along x in a non-equilibrium boundary layer. Note that due to the use of local plus units in y_w^+ and U^+ , etc., the present modification needs special treatment at the separation point and inside the separated flow region, which will be discussed later. To determine $\kappa(x)$, the diagnostic function $I(x, y) = y^+ \partial U^+ / \partial y^+$ (Figure 12(b)) is calculated from the mean velocity profile (Figure 12(a)) for data of Wu *et al.* (2019). The local minima of $I(x, y)$ at a given x is taken as $1/\kappa(x)$. Following the determination of $\kappa(x)$, $B(x)$ is calculated using $U^+(x, y) - [\kappa(x)^{-1} \log y^+ + B(x)] = 0$. Figure 12(d) shows that the correlation between $\kappa(x)$ and $B(x)$ obtained for all cases in the present datasets in the attached flow regions is consistent with that observed by Nagib & Chauhan (2008) and Nickels (2004) from a large collection of flows with or without pressure gradients. As shown in Figure 10(c) compared to Figure 10(b), the modeling of overlap-range width based on y_w^+ is successful for the present APG datasets: the high-frequency range is now better predicted with the corrected width. The main WPS prediction error is now

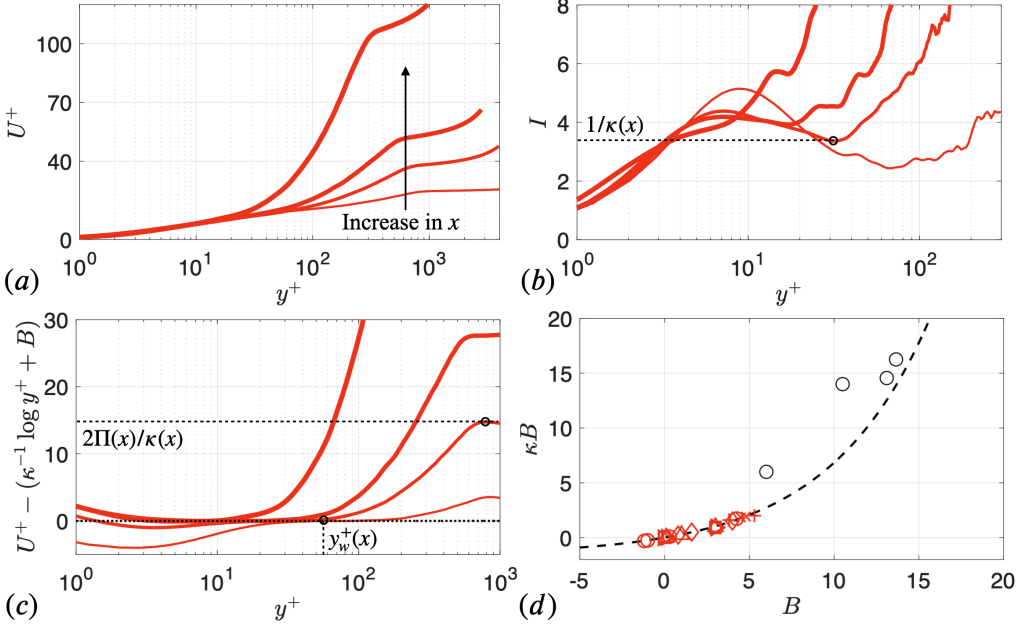


FIGURE 12. (a-c) Calculation of $\kappa(x)$, $B(x)$ and model parameters shown using Wu *et al.* (2019) data at locations $x/\theta_o = 50, 105, 120$ and 130 . (a) Mean velocity profiles in inner units. Increasing line thickness indicates increase in x . (b) Diagnostic function, $I = y^+ \partial U^+ / \partial y^+$. (c) Velocity profiles with logarithmic relation subtracted. Calculations of κ , Π and y_w^+ are indicated for $x/\theta_o = 105$ in (b,c). (d) Correlation between calculated κB and B , compared to the fitted relation from Nagib & Chauhan (2008) (---): \circ Wu & Piomelli (2018) (attached flow before separation), \circ Wu & Piomelli (2018) (attached flow downstream of reattachment), \diamond Hu (2018), \times Fritsch *et al.* (2022a), $+$ Goody (2004), \square Pargal *et al.* (2022), \triangleright Wu *et al.* (2019) and \triangle Na & Moin (1998).

predominantly an inaccurate slope of the overlap range, as shown in Figure 10(c).

Recognizing that an APG leads to more energized large turbulence motions in the outer layer and a thinner logarithmic layer, the change in WPS overlap-range slope (in addition to the change of the width of this range as is characterized by y_w^+) is assumed to be caused by the variation in the strength of the outer-layer turbulent motions. To account for the variation in the strength of the wake region, an additional model input is used: Coles' parameter, $\Pi(x)$. An augmentation of Π signals stronger turbulent intensity and mixing in the outer layer. Here, $\Pi(x)$ is evaluated based on $U^+(x, y)$, by measuring the peak value of $U^+ - [\kappa^{-1}(\log(y^+) + B)]$ (as shown in Figure 12(c)) and dividing it by $2/\kappa(x)$. In the generic model form in Equation (5.2), the coefficient c is known to impose the slope of the overlap range of ϕ_{pp} (Thomson & Rocha 2022; Lee 2018; Rozenberg *et al.* 2012). Therefore, the constant c is replaced by a function of both Π and y_w^+ , fitted

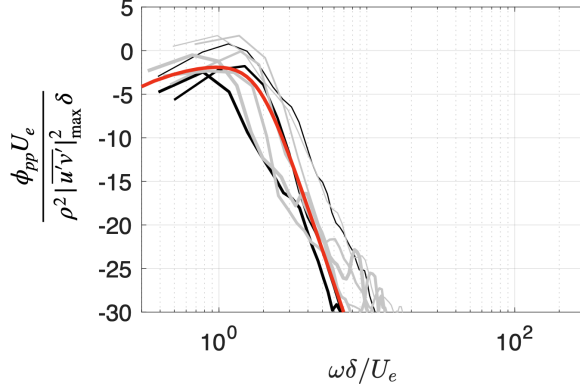


FIGURE 13. Comparison between model prediction (—) and simulation data (— Na & Moin (1998) and — Wu & Piomelli (2018)) in the separated-flow regions. Increasing line thickness indicates an increase in x as marked in Figure 8(a).

based on the present datasets. To keep the model stable, especially in cases with extreme pressure gradient or in the region near flow separation, c is limited to a maximum value of 1. The final form of the generalized WPS model is

$$\frac{\phi_{pp}(\omega)U_e}{(\rho|u'v'|_{\max})^2\delta} = \frac{3(\omega\delta/U_e)^2}{[(\omega\delta/U_e)^c + 0.7]^{3.7} + [(y_w^+)^{-0.37}(\omega\delta/U_e)]^7}, \quad \text{where} \quad (5.3)$$

$$c = \min [1, 0.8 + 3.34e^{-4}\Pi^{1.86}(y_w^+)^{0.76}]. \quad (5.4)$$

Figure 10(d) shows that the generalized model predicts the WPS very well in both ZPG and strong-APG flows in the present datasets. Note, however, that the present strong-APG data used to calibrate this model are from limited-Reynolds-number flows with a rather narrow WPS overlap range. Additional data from high-Reynolds-number strong-APG flows are not available, but are needed to validate the use of the model of its present form in flows with higher Reynolds numbers.

A few scenarios require special treatments as listed in Table 4. For cases with very low Reynolds numbers with extreme adverse pressure gradient which practically removes the logarithmic region from the boundary layer (i.e. if $y_w^+ < 15$), y_w^+ and c are set to constant values: $y_w^+ = 15$ and $c = 0.85$ as calibrated from the present datasets, to reflect the insensitivity of ϕ_{pp} to either Reynolds number or pressure gradient as shown in Figure 7(a). Moreover, in case of boundary layer separation, modification of the model is needed for x locations at the separation point and inside the separation bubble.

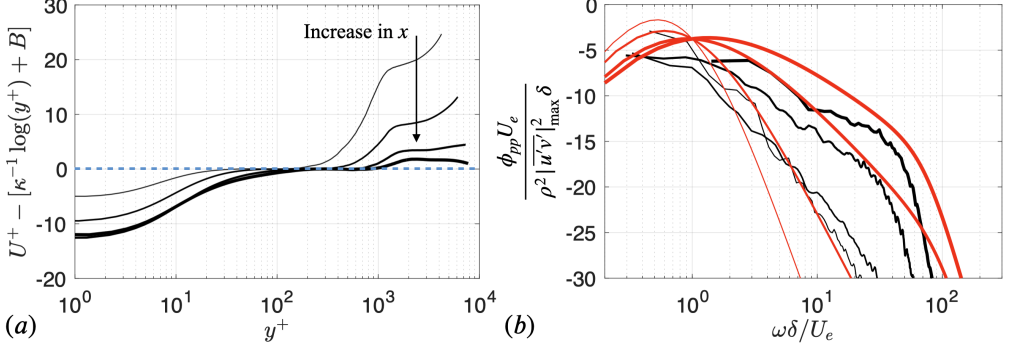


FIGURE 14. Comparison between model prediction (—) and Wu & Piomelli (2018) data (—) in the attached-flow region downstream of reattachment point (at x/θ_o from 250 to 350, the most downstream location corresponding to near equilibrium flow). (a) Mean velocity profiles with the logarithmic relation subtracted; --- value corresponding to logarithmic layer. (b) Wall-pressure PSD comparison. Increasing line thickness indicates an increase in x .

Inspired by the almost identical WPS profile across the normalized frequency range in the separated region as shown in Figure 8(b), y_w^+ and c are set to constants: $y_w^+ = 2$, $c = 0.75$, and d is set to 0.5 (Table 4), calibrated based on the data of Na & Moin (1998) and Wu & Piomelli (2018). The separation modification is activated for x regions where $C_f(x)$ is calculated as zero or negative, corresponding to the region of mean-flow separation. With the above-mentioned separated-flow treatment, the proposed model is evaluated at a number of streamwise locations inside the separation regions of the flows of Na & Moin (1998) and Wu & Piomelli (2018) in Figure 13. The WPS prediction does not vary with x in this region, since the model parameters are set to constants. Good comparison with the simulation data is achieved. Although the separation treatment introduces a discontinuity in c value at the separation point (as c approaches 1 towards the point while $c = 0.75$ at that point), it is shown not to affect the prediction significantly, as the overlap range is short in the strong-APG region in the vicinity of the detachment.

Although the model is primarily developed for attached or separated APG flows, it is examined in other regions of a non-equilibrium boundary layer to explore its extendibility to more universal applications. First, the model is evaluated in the region downstream from the flow reattachment point till a near-equilibrium ZPG state in Figure 14 against Wu & Piomelli (2018) data, at four x locations between $x/\theta_o = 250$ and $x/\theta_o = 350$. Figure 14(a) shows that, near the reattachment point (shown by the thinnest lines), the local mean velocity departs significantly from a canonical boundary layer profile,

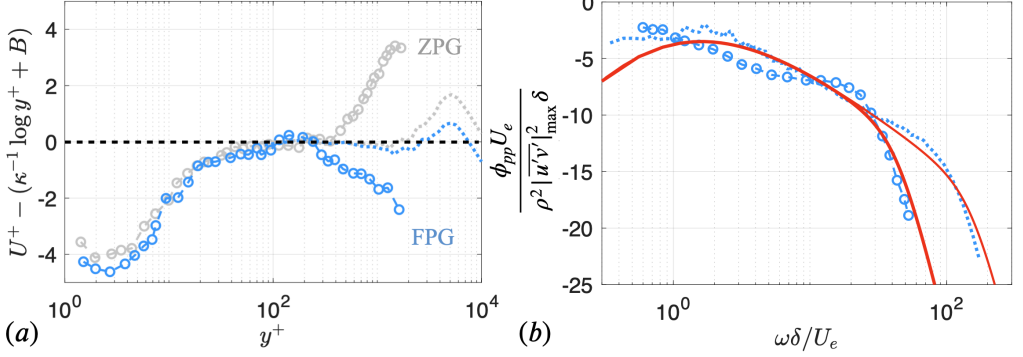


FIGURE 15. Comparison between model prediction (—) and experimental data in FPG flows (Hu 2018; Fritsch *et al.* 2022b). For legend see Table 2. (a) Mean velocity profile with the logarithmic relation subtracted; FPG and ZPG states are shown in blue and gray, respectively. --- Value corresponding to logarithmic layer. (b) Wall-pressure PSD comparison.

without a clear logarithmic layer. With increasing x , the logarithmic layer gradually recovers towards the equilibrium ZPG state and the overlap range of the WPS thickens gradually (Figure 14 (b)). The model is shown to capture such trend of WPS variation. The overall spectral levels are well predicted due to the approximate scaling of p_{rms} on $\rho |\overline{u'v'}|_{\max}$, while the spectral shape is captured by $y_w^+(x)$ and $\Pi(x)$ representing the local thickening of the logarithmic layer and the weakening of wake, respectively, during recovery.

In addition, the model is tested in FPG flows as shown in Figure 15, against the experimental data of Hu (2018) and Fritsch *et al.* (2022b). Figure 15(a) shows that, under FPGs (shown in blue) as compared to the ZPG profiles (shown in gray), the main change is a reduction of Π , which leads to a milder slope of the WPS overlap range. Figure 15(b) shows that this change in WPS is globally captured well by the proposed model.

Figure 16 shows results of sensitivity analyses carried out for the parameters y_w^+ and Π of the proposed model. The WPS predictions obtained with $\pm 30\%$ change of each of the two parameters (marked by the highlighted region) are compared with the datasets, for three types of flows with different ranges of Reynolds number and β . Figures 16(a,c,e) show that the variation of y_w^+ has an effect on the overlap-range and high-frequency contents, by controlling the width of the overlap range. The effect appears to be particularly strong in a weak-APG flow. Figures 16(b,d,f) show that $\Pi(x)$

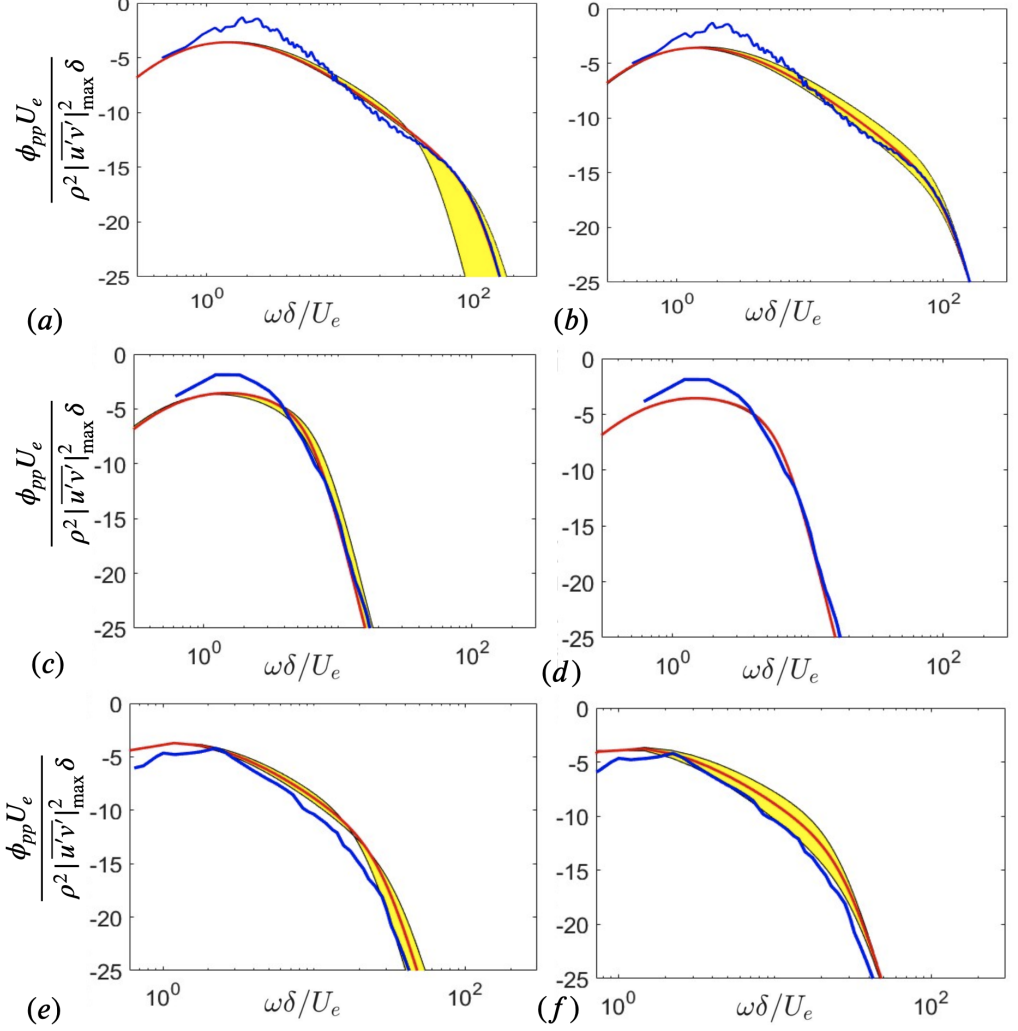


FIGURE 16. WPS prediction of the proposed model (—) compared to measurements (—) in the following cases: (a,b) high-Reynolds-number and low-APG flow (Fritsch *et al.* 2022b, $\beta = 0.58$), (c,d) low-Reynolds-number and strong-APG flow (Wu *et al.* 2019, $\beta = 8.3$), and (e,f) high-Reynolds-number and strong-APG flow (Hu 2018, $\beta = 6$). Yellow regions mark prediction variations with $\pm 30\%$ change in input parameters y_w^+ (a,c,e) or II (b,d,f). In (d), variation of II does not change WPS prediction as c is set to a constant at this location due to $y_w^+ < 15$ (see Table 4).

modifies the slope of the overlap range, with the model particularly sensitive to its value in high-Reynolds-number flows where the overlap range is pronounced. These results show that the introduced parameters affect the WPS prediction in their intended ways. Furthermore, slight variations in quantifying y_w^+ and II do not significantly worsen WPS prediction.

6. Conclusions and discussions

In this study, datasets collected from numerical (DNS and LES) and experimental studies are used to characterize the variation of wall-pressure statistics in various types of boundary layer flows, attached or separated and then reattached, with zero, adverse or favorable pressure gradients at different ranges of Reynolds number. The numerical data in the datasets were validated in various flow quantities. They are not prone to errors originating from installation effects as in many experimental studies and are free from modeling errors as in RANS or boundary layer closures used in the development of some existing WPS models. Strongly non-equilibrium streamwise pressure gradient variations are included in the datasets. By comparing different sets of variables used to normalize the wall-pressure spectrum (ϕ_{pp}), an optimal set of scaling is identified: U_e , δ and $\rho|\overline{u'v'}|_{\max}$, and is used for wall-pressure spectrum model development.

The performances of various existing wall-pressure spectrum models are evaluated in the flows contained in the datasets. These models are shown to fail to predict the wall-pressure spectra in non-equilibrium strong-APG flows. The failures are caused by the use of inappropriate pressure scaling (τ_w), being fitted to limited types of flows, and the dependencies on u_τ -based model parameters, as u_τ reduces to zero at the detachment point.

Next, more robust model parameters are proposed and used to modify Goody's model. These parameters are (i) the logarithmic-layer extent, y_w^+ , and (ii) Coles' parameter, Π . These parameters carry information on the local state of the boundary layer flow as carried in the mean velocity profile. The parameters are quantifiable from Reynolds-averaged Navier-Stokes (RANS) calculation of the mean velocity. This is a more direct approach to model the change in contributions of wall-layer and outer-layer turbulent flows to the wall-pressure spectrum, compared to existing approaches based on local pressure gradient (e.g. Clauser's parameter, β) and/or local Reynolds number (e.g. R_t). In addition, y_w^+ and Π capture the history effect of non-equilibrium pressure gradients as recorded in the velocity prediction (from a RANS simulation, for example), which is not directly represented by the local pressure gradient.

Comparison with available numerical and experimental measurements shows that the

proposed model gives good predictions for ZPG, APG (attached-flow region) and FPG flows. For strong APG flows with boundary-layer separation and reattachment, the wall-pressure spectra are shown to display similar shapes and magnitudes across the separation bubble. There, the model is shown to give overall good predictions, if the overlap-range width and slope are set to constants fitted based on present data. A qualitatively good prediction is also obtained downstream of flow reattachment where the boundary layer departs significantly from its equilibrium state. Hence, the new model is considered as a generalized wall-pressure spectral model for a wide range of equilibrium and non-equilibrium boundary layers, as opposed to existing models designed for limited types of flows.

Acknowledgments

SP is grateful for the funding provided by the Consortium for the Development of Ultra-High Efficiency Quiet Fans at Université de Sherbrooke. SP and JY also gratefully acknowledge the additional financial support by Office of Naval Research (Award No. N00014-17-1-2102). Computational support was provided by Michigan State University's Institute for Cyber-Enabled Research and the Digital Research Alliance of Canada.

Declaration of interests

The authors report no conflict of interest.

REFERENCES

- ABE, H. 2017 Reynolds-number dependence of wall-pressure fluctuations in a pressure-induced turbulent separation bubble. *Journal of Fluid Mechanics* **28** (4), 719–754.
- AMIET, R. K. 1976 Noise due to turbulent flow past a trailing edge. *Journal of Sound and Vibration* **47** (3), 387–393.
- AVALLONE, F., VAN DER VELDEN, W. C. P., RAGNI, D. & CASALINO, D. 2018 Noise reduction mechanisms of sawtooth and combed-sawtooth trailing-edge serrations. *Journal of Fluid Mechanics* **848**, 560–591.
- BLAKE, WILLIAM K 1970 Turbulent boundary-layer wall-pressure fluctuations on smooth and rough walls. *Journal of Fluid Mechanics* **44** (4), 637–660.

- BORELLI, DAVIDE, GAGGERO, TOMASO, RIZZUTO, ENRICO & SCHENONE, CORRADO 2021 Onboard ship noise: Acoustic comfort in cabins. *Applied Acoustics* **177**, 107912.
- BULL, M. K. 1996 Wall-pressure fluctuations beneath turbulent boundary layers: Some reflections on forty years of research. *Journal of Sound and Vibration* **190** (3), 299–315.
- BULL, M. K. & THOMAS, A. S. W. 1976 High frequency wall-pressure fluctuations in turbulent boundary layers. *Physics of Fluids* **19** (4), 597–599.
- CAIAZZO, A., PARGAL, S., WU, H., SANJOSÉ, M., YUAN, J. & MOREAU, S. 2023 On the effect of adverse pressure gradients on wall-pressure statistics in a controlled-diffusion aerofoil turbulent boundary layer. *Journal of Fluid Mechanics* **960**, A17.
- CARPENTER, M. H., NORDSTRÖM, J. & GOTTLIEB, D. 1999 A stable and conservative interface treatment of arbitrary spatial accuracy. *J. Comp. Phys.* **148**, 341–365.
- CASALINO, D., GRANDE, E., ROMANI, G., RAGNI, D & AVALLONE, F 2021 Towards the definition of a benchmark for low Reynolds number propeller aeroacoustics. In *Journal of Physics: Conference Series*, , vol. 1909, p. 012013. IOP Publishing.
- CATLETT, M. R., ANDERSON, J. M., FOREST, J. B. & STEWART, D. O. 2016 Empirical modeling of pressure spectra in adverse pressure gradient turbulent boundary layers. *AIAA Journal* **54** (2), 569–587.
- CELIK, A., JAMALUDDIN, N. S., BASKARAN, K., REZGUI, D. & AZARPEYVAND, M. 2021 Aeroacoustic performance of rotors in tandem configuration. In *AIAA AVIATION 2021 Forum*, p. 2282.
- CHANG III, P. A., PIOMELLI, U. & BLAKE, W. K. 1999 Relationship between wall pressure and velocity-field sources. *Physics of Fluids* **11** (11), 3434–3448.
- CHASE, D. M. 1980 Modeling the wavevector-frequency spectrum of turbulent boundary layer wall pressure. *Journal of Sound and Vibration* **70** (1), 29–67.
- CLAUSER, F. H. 1954 Turbulent boundary layers in adverse pressure gradients. *Journal of the Aeronautical Sciences* **21** (2), 91–108.
- COHEN, E. & GLOERFELT, X. 2018 Influence of pressure gradients on wall pressure beneath a turbulent boundary layer. *Journal of Fluid Mechanics* **838**, 715–758.
- COLES, D. 1956 The law of the wake in the turbulent boundary layer. *Journal of Fluid Mechanics* **1** (2), 191–226.
- CORCOS, G. M. 1964 The structure of the turbulent pressure field in boundary-layer flows. *Journal of Fluid Mechanics* **18** (3), 353–378.
- DESHMUKH, S., BHATTACHARYA, S., JAIN, A. & PAUL, A. R. 2019 Wind turbine noise and its mitigation techniques: A review. *Energy Procedia* **160**, 633–640.
- DOMINIQUE, J., VAN DEN BERGHE, J., SCHRAM, C. & MENDEZ, M. A. 2022 Artificial neural

- networks modeling of wall pressure spectra beneath turbulent boundary layers. *Physics of Fluids* **34** (3), 035119.
- DRELA, M. 1989 XFOIL: an analysis and design system for low Reynolds number airfoils. In *Low Reynolds number aerodynamics* (ed. T. J. Mueller), *Lecture Notes in Engineering*, vol. 54, pp. 1–12. Berlin: Springer-Verlag.
- FARABEE, T. M. & CASARELLA, M. J. 1991 Spectral features of wall pressure fluctuations beneath turbulent boundary layers. *Physics of Fluids A: Fluid Dynamics* **3** (10), 2410–2420.
- FRANCO, F., BERRY, A., PETRONE, G., DE ROSA, S., CIAPPI, E. & ROBIN, O. 2020 Structural response of stiffened plates in similitude under a turbulent boundary layer excitation. *Journal of Fluids and Structures* **98**, 103119.
- FRITSCH, D. J., VISHWANATHAN, V., ROY, C. J., TODD LOWE, K., DEVENPORT, W. J., CROAKER, P., LANE, G., TKACHENKO, O., POOK, D., SHUBHAM, S. & OTHERS 2022a Modeling the surface pressure spectrum beneath turbulent boundary layers in pressure gradients. In *28th AIAA/CEAS Aeroacoustics 2022 Conference*, p. 2843.
- FRITSCH, D. J., VISHWANATHAN, V., TODD LOWE, K. & DEVENPORT, W. J. 2022b Fluctuating pressure beneath smooth wall boundary layers in nonequilibrium pressure gradients. *AIAA Journal* pp. 1–19.
- GERMANO, M., PIOMELLI, U., MOIN, P. & CABOT, W. H. 1991 A dynamic subgrid-scale eddy viscosity model. *Phys. Fluids A* **3**, 1760–1765.
- GHIGLINO, A., PULLIN, S. F., ZHOU, B. Y., ABID, H. & KARABASOV, S. A. 2023 Towards an adaptive trailing-edge noise model using a data-driven approach. In *AIAA AVIATION 2023 Forum*, p. 4371.
- GOODY, M. 2004 Empirical spectral model of surface pressure fluctuations. *AIAA Journal* **42** (9), 1788–1794.
- GOODY, M. C. & SIMPSON, R. L. 2000 Surface pressure fluctuations beneath two- and three-dimensional turbulent boundary layers. *AIAA Journal* **38** (10), 1822–1831.
- GRASSO, G., ROGER, M. & MOREAU, S. 2022 Advances in the prediction of the statistical properties of wall-pressure fluctuations under turbulent boundary layers. *Fluids* **7** (5), 161.
- HALES, A. & AYTON, L. J. 2023 Adapting a trailing-edge noise model to an impedance boundary condition. In *AIAA AVIATION 2023 Forum*, p. 3821.
- HU, N. 2018 Empirical model of wall pressure spectra in adverse pressure gradients. *AIAA Journal* **56** (9), 3491–3506.
- HU, N., BUCHHOLZ, H., HERR, M., SPEHR, C. & HAXTER, S. 2013 Contributions of

- different aeroacoustic sources to aircraft cabin noise. In *19th AIAA/CEAS Aeroacoustics Conference*, p. 2030.
- HU, N. & HERR, M. 2016 Characteristics of wall pressure fluctuations for a flat plate turbulent boundary layer with pressure gradients. In *22nd AIAA/CEAS Aeroacoustics Conference, Lyon, France*, pp. 2749–2767.
- JAISWAL, P., MOREAU, S., AVALLONE, F., RAGNI, D. & PRÖBSTING, S. 2020 On the use of two-point velocity correlation in wall-pressure models for turbulent flow past a trailing edge under adverse pressure gradient. *Physics of Fluids* **32** (10), 105105.
- JI, M. & WANG, M. 2012 Surface pressure fluctuations on steps immersed in turbulent boundary layers. *Journal of Fluid Mechanics* **712**, 471–504.
- JONES, L. E., SANDBERG, R. D. & SANDHAM, N. D. 2008 Direct numerical simulations of forced and unforced separation bubbles on an airfoil at incidence. *J. Fluid Mech.* **602**, 175–207.
- KAMRUZZAMAN, M., BEKIROPOULOS, D., LUTZ, T., WÜRZ, W. & KRÄMER, E. 2015 A semi-empirical surface pressure spectrum model for airfoil trailing-edge noise prediction. *International Journal of Aeroacoustics* **14** (5-6), 833–882.
- KENNEDY, C. A., CARPENTER, M. H. & LEWIS, R. M. 1999 Low-storage, explicit Runge-Kutta schemes for the compressible Navier-Stokes equations. *Applied Numerical Mathematics* **35**, 177–219.
- KRAICHNAN, R. H. 1956 Pressure fluctuations in turbulent flow over a flat plate. *The Journal of the Acoustical Society of America* **28** (3), 378–390.
- LALLIER-DANIELS, D., BOLDUC-TEASDALE, F., RANCOURT, D. & MOREAU, S. 2021 Fast multi-objective aeroacoustic optimization of propeller blades. In *Vertical Flight Society's 77th Annual Forum & Technology Display*.
- LAUZON, J.-S., VINCENT, J., PASCO, Y., GRONDIN, F. & MOREAU, S. 2023 Aeroacoustics of drones. In *AIAA AVIATION 2023 Forum*, p. 4524.
- LEE, S. 2018 Empirical wall-pressure spectral modeling for zero and adverse pressure gradient flows. *AIAA Journal* **56** (5), 1818–1829.
- LEE, S., AYTON, L., BERTAGNOLIO, F., MOREAU, S., CHONG, T. P. & JOSEPH, P. 2021 Turbulent boundary layer trailing-edge noise: Theory, computation, experiment, and application. *Progress in Aerospace Sciences* **126**, 100737.
- LILLY, D. K. 1992 A proposed modification of the Germano subgrid-scale closure method. *Phys. Fluids A* **4**, 633–635.
- LUND, T. S., WU, X. & SQUIRES, K. D. 1998 Generation of turbulent inflow data for spatially-

- developing boundary layer simulations. *Journal of Computational Physics* **140** (2), 233–258.
- LUO, B., CHU, W. & ZHANG, H. 2020 Tip leakage flow and aeroacoustics analysis of a low-speed axial fan. *Aerospace Science and Technology* **98**, 105700.
- MENEVEAU, C., LUND, T. S. & CABOT, W. H. 1996 A Lagrangian dynamic subgrid-scale model of turbulence. *J. Fluid Mech.* **319**, 353–385.
- MOREAU, S. & ROGER, M. 2009 Back-scattering correction and further extensions of Amiet’s trailing-edge noise model. Part II: Application. *Journal of Sound and Vibration* **323** (1-2), 397–425.
- NA, Y & MOIN, PARVIZ 1998 The structure of wall-pressure fluctuations in turbulent boundary layers with adverse pressure gradient and separation. *Journal of Fluid Mechanics* **377**, 347–373.
- NAGIB, H. M. & CHAUHAN, K. A. 2008 Variations of von Kármán coefficient in canonical flows. *Physics of Fluids* **20**, 101518.
- NICKELS, T. B. 2004 Inner scaling for wall-bounded flows subject to large pressure gradients. *Journal of Fluid Mechanics* **521**, 217–239.
- ORLANSKI, I 1976 A simple boundary condition for unbounded hyperbolic flows. *Journal of Computational Physics* **21** (3), 251–269.
- PALANI, S., PARUCHURI, C. C., JOSEPH, P., KARABASOV, S. A., MARKESTEIJN, A., ABID, H., CHONG, T. P. & UTUZHNIKOV, S. 2023 Modified TNO-Blake model for aerofoil surface pressure prediction with canopies. In *AIAA AVIATION 2023 Forum*, p. 3203.
- PANTON, R. L. & LINEBARGER, J. H. 1974 Wall pressure spectra calculations for equilibrium boundary layers. *Journal of Fluid Mechanics* **65** (2), 261–287.
- PARGAL, S., LI, W. & LI, Y. 2023 Large Eddy Simulation of non-equilibrium flows using Lattice Boltzmann method. In *AIAA SCITECH 2023 Forum*, p. 2149.
- PARGAL, S., WU, H., YUAN, J. & MOREAU, S. 2022 Adverse-pressure-gradient turbulent boundary layer on convex wall. *Physics of Fluids* **34** (3), 035107.
- ROGER, M. & MOREAU, S. 2005 Back-scattering correction and further extensions of Amiet’s trailing-edge noise model. Part 1: theory. *Journal of Sound and Vibration* **286** (3), 477–506.
- ROSSI, T. & SAGAUT, P. 2023 Prediction of wall-pressure spectra for separated/reattached boundary layer flows. In *AIAA AVIATION 2023 Forum*, p. 3338.
- ROZENBERG, Y., ROBERT, G. & MOREAU, S. 2012 Wall-pressure spectral model including the adverse pressure gradient effects. *AIAA Journal* **50** (10), 2168–2179.
- SAMARASINGHE, P. N., ZHANG, W. & ABHAYAPALA, T. D. 2016 Recent advances in active noise

- control inside automobile cabins: Toward quieter cars. *IEEE Signal Processing Magazine* **33** (6), 61–73.
- SANDBERG, R. D. 2015 Compressible-flow DNS with application to airfoil noise. *Flow, Turb. Comb.* **95**, 211–229.
- SANDBERG, R. D. & SANDHAM, N. D. 2006 Nonreflecting zonal characteristic boundary condition for direct numerical simulation of aerodynamic sound. *AIAA J.* **44**, 402–405.
- SANJOSÉ, M. & MOREAU, S. 2018 Fast and accurate analytical modeling of broadband noise for a low-speed fan. *The Journal of the Acoustical Society of America* **143** (5), 3103–3113.
- SCHLOEMER, H. H. 1967 Effects of pressure gradients on turbulent-boundary-layer wall-pressure fluctuations. *The Journal of the Acoustical Society of America* **42** (1), 93–113.
- SHUBHAM, S., PARGAL, S., MOREAU, S., SANDBERG, R. D., YUAN, J., KUSHARI, A. & SANJOSE, M. 2023 Data-driven empirical wall pressure spectrum models for fan noise prediction. In *AIAA AVIATION 2023 Forum*, p. 3508.
- SIMPSON, R. L., GHODBANE, M. & MCGRATH, B. E. 1987 Surface pressure fluctuations in a separating turbulent boundary layer. *Journal of Fluid Mechanics* **177**, 167–186.
- SWANEPOEL, P. C., BIEDERMANN, T. M. & VAN DER SPUY, S. J. 2023 Experimental noise reduction (aeroacoustical enhancement) of a large diameter axial flow cooling fan through a reduction in blade tip clearance. *International Journal of Aeroacoustics* p. 1475472X231183156.
- THOMSON, N. & ROCHA, J. 2022 Semi-empirical wall pressure spectral modeling for zero and favorable pressure gradient flows. *The Journal of the Acoustical Society of America* **152** (1), 80–98.
- VAN BLITTERSWYK, J. & ROCHA, J. 2017 An experimental study of the wall-pressure fluctuations beneath low Reynolds number turbulent boundary layers. *The Journal of the Acoustical Society of America* **141** (2), 1257–1268.
- VENKATRAMAN, K., MOREAU, S., CHRISTOPHE, J. & SCHRAM, C. F. 2023 Numerical investigation of aerodynamics and aeroacoustics of helical Darrieus wind turbines. In *AIAA AVIATION 2023 Forum*, p. 3641.
- WILLMARTH, W. W. 1975 Pressure fluctuations beneath turbulent boundary layers. *Annual Review of Fluid Mechanics* **7** (1), 13–36.
- WU, H., MOREAU, S. & SANDBERG, R. D. 2019 Effects of pressure gradient on the evolution of velocity-gradient tensor invariant dynamics on a controlled-diffusion aerofoil at $Re_c = 150000$. *Journal of Fluid Mechanics* **868**, 584–610.
- WU, W. & PIOMELLI, U. 2018 Effects of surface roughness on a separating turbulent boundary layer. *Journal of Fluid Mechanics* **841**, 552–580.